coatings

MDPI

Article

Insights in to the Electrochemical Activity of Fe-Based Perovskite Cathodes toward Oxygen Reduction Reaction for Solid Oxide Fuel Cells

Dan Ma, Juntao Gao, Tian Xia, Qiang Li *, Liping Sun, Lihua Huo and Hui Zhao

Key Laboratory of Functional Inorganic Material Chemistry, Ministry of Education, School of Chemistry and Materials Science, Heilongjiang University, Harbin 150080, China; madan18845166284@hotmail.com (D.M.); 20b911032@stu.hit.edu.cn (J.G.); xiatian@hlju.edu.cn (T.X.); sunliping@hlju.edu.cn (L.S.); huolihua@hlju.edu.cn (L.H.); zhaohui@hlju.edu.cn (H.Z.)

* Correspondence: liqiang@hlju.edu.cn

Received: 27 November 2020; Accepted: 18 December 2020; Published: 19 December 2020

Abstract: The development of novel oxygen reduction electrodes with superior electrocatalytic activity and CO_2 durability is a major challenge for solid oxide fuel cells (SOFCs). Here, novel cobalt-free perovskite oxides, $BaFe_{1-x}Y_xO_{3-\delta}$ (x = 0.05, 0.10, and 0.15) denoted as BFY05, BFY10, and BFY15, are intensively evaluated as oxygen reduction electrode candidate for solid oxide fuel cells. These materials have been synthesized and the electrocatalytic activity for oxygen reduction reaction (ORR) has been investigated systematically. The BFY10 cathode exhibits the best electrocatalytic performance with a lowest polarization resistance of 0.057 Ω cm^2 at 700 °C. Meanwhile, the single cells with the BFY05, BFY10 and BFY15 cathodes deliver the peak power densities of 0.73, 1.1, and 0.89 W cm^{-2} at 700 °C, respectively. Furthermore, electrochemical impedance spectra (EIS) are analyzed by means of distribution of relaxation time (DRT). The results indicate that the oxygen adsorption-dissociation process is determined to be the rate-limiting step at the electrode interface. In addition, the single cell with the BFY10 cathode exhibits a good long-term stability at 700 °C under an output voltage of 0.5 V for 120 h.

Keywords: solid oxide fuel cells; oxygen reduction electrode; electrocatalytic activity

1. Introduction

Perovskite-type materials are the promising cathodes for solid oxide fuel cells (SOFCs) [1–3]. Among the perovskite oxides, the Co-containing perovskite materials with mixed ionic-electronic conducting feature have been widely investigated due to their remarkable electrochemical performance for ORR [4–6]. However, Co-containing oxides show some other drawbacks, such as poor chemical stability, higher thermal expansion coefficient, and strong volatility, which inhibit their wide applications in SOFCs [7,8]. To address these issues, developing new cathodes with improved electrochemical performance and good chemical stability is an important trend. Recently, Fe-based perovskite materials exhibit attractive chemical compatibility and excellent electrocatalytic activity, such as $SrFe_{1-x}Ti_xO_{3-\delta}$, $SrFe_{0.8}Nb_{0.2-x}Ta_xO_{3-\delta}$, $La_{1-x}Sr_xFeO_{3-\delta}$, and $Ba_{1-x}La_xFeO_{3-\delta}$ [9–12].

Among the Fe-based oxides, $BaFeO_{3-\delta}$ presents attractive oxygen permeation flux and fast oxygen surface exchange kinetics [13,14]. This is mainly due to variable valence and excellent chemical stability of Fe ions, as well as lower valence and larger ionic radius of Ba^{2+}, which facilitates the electrochemical performance and oxygen transport of the materials [15]. Cation-doping is commonly adopted to stabilize the cubic lattice of $BaFeO_{3-\delta}$ with disordered oxygen vacancies, such as La^{3+}, Sm^{3+}, and Ca^{2+} in the A site and Nb^{5+}, Sn^{4+}, In^{3+}, and Ni^{2+} in the B site [12,16–18]. Lu et al. found that In^{3+} doping

in the B site of $BaFeO_{3-\delta}$ can enhance oxygen permeation flux, in which $BaFe_{0.9}In_{0.1}O_{3-\delta}$ presented the higher oxygen permeation flux of 1.11 mL cm^{-2} min^{-1} at 950 °C [19]. Song et al. reported an attractive cathode candidate of $BaFe_{1-x}Bi_xO_{3-\delta}$ for SOFCs. The $BaFe_{0.9}Bi_{0.1}O_{3-\delta}$ cathode exhibited a lower polarization resistance of 0.133 Ω cm^2 at 750 °C and a high oxygen vacancy concentration of 0.408. However, the thermal expansion coefficient of $BaFe_{0.9}Bi_{0.1}O_{3-\delta}$ is very large (26.697×10^{-6} K^{-1}). Additionally, the oxygen permeability and oxygen non-stoichiometry of $BaFe_{1-x}Y_xO_{3-\delta}$ have been investigated by Liu et al. They found that Y-doping promotes the oxygen vacancy concentration and oxygen ion migration, which is believed to be favorable for transport of the oxygen ion in the bulk electrode, thereby resulting in the enhanced electrocatalytic performance [20].

In this work, Fe-based perovskite $BaFe_{1-x}Y_xO_{3-\delta}$ oxides have been investigated as the prominent cathodes for SOFCs. The crystalline structure, CO_2 tolerance, and electrocatalytic activity for ORR of the $BaFe_{1-x}Y_xO_{3-\delta}$ cathodes are systematically investigated. The results provide an effective strategy for designing novel cathode electrocatalysts for SOFCs.

2. Experimental

2.1. Material Preparation

The $BaFe_{1-x}Y_xO_{3-\delta}$ (x = 0.05–0.15) samples were synthesized by the solid-state reaction. Stoichiometric amounts of $BaCO_3$ (99.99%, Tianjin Guangfu Co. Ltd., Tianjin, China), Fe_2O_3 (99.99%, Tianjin Guangfu Co. Ltd.), and Y_2O_3 (99.99%, Tianjin Guangfu Co. Ltd.) were mixed and ground via the ball milling using ethanol as the dispersant. Afterwards, the mixture was pre-fired at 1000 °C for 10 h with a heating rate of 5 °C min^{-1} in air and then re-milled for 1 h, followed by calcining at 1300 °C for 12 h to obtain the final products.

2.2. Characterization

The crystal structure of BFYx cathodes were identified using X-ray diffraction (Bruker D8 advance) with filtered Cu-Kα radiation (λ = 1.5148 Å) source in a 2θ range of 10°–80°. The XRD data was analyzed to obtain the structural parameters by using Rietveld refinement method using the Rietica software (Version 1.7.7.8) program. The oxygen desorption property of the cathode catalysts was carried out by O_2 temperature-programmed desorption (O_2-TPD) with the TP-5076 instrument (Tianjin Xianquan, Co. Ltd., Tianjin, China). The electrical conductivity was measured between 100 and 800 °C in air by standard four-probe DC method with a Keithley 2400 SourceMeter Keithley Instruments Inc., Cleveland, OH, USA). The oxygen non-stoichiometry of the samples at room temperature was determined with the iodometric titration method, as described elsewhere [21,22]. The oxygen non-stoichiometry at high temperature was measured by thermogravimetric analysis (TGA, SETARAM, Caluire et Cuire, France).

2.3. Electrochemical Test

The dense $Ce_{0.9}Gd_{0.1}O_{1.95}$ (CGO) electrolyte was fabricated by pressing CGO powders (SOFCMAN Co. Ltd., Ningbo, China) uniaxially at 220 MPa, and sintered at 1450 °C for 24 h. For the fabrication of symmetrical cells (BFYx|CGO|BFYx), the BFYx electrode powders were mixed with terpineol and ethyl cellulose to prepare the cathode slurry. The slurry was symmetrically coated on the $Ce_{0.9}Gd_{0.1}O_{2-\delta}$ (CGO) electrolyte and sintered at 900 °C for 4 h. The electrochemical impedance spectroscopy (EIS) of symmetric cell was acquired by an Autolab PGSTAT302N workstation in the frequency range of 10^{-2}–10^6 Hz under open voltage conditions at 500–700 °C. To explore the electrochemical process for ORR of the electrode, the EIS spectra were collected under different oxygen partial pressure (PO_2).

The anode-supported half cell (NiO-YSZ|YSZ|CGO) was bought from Ningbo SuoFuRen Energy Co. Ltd. (Ningbo, China). The BFYx cathode slurry was printed onto the CGO barrier layer, and subsequently co-fired at 900 °C for 4 h. The electrochemical performance of anode-supported fuel cells was tested using electrochemical workstation (ZAHNER, IM6e, Kronach, Germany. The single cell

was mounted on the alumina tube, while the humidified H_2 (3% H_2O) with a flow rate of 80 mL min^{-1} and ambient air were used as the fuel and oxidant, respectively.

3. Results and Discussion

Figure 1a displays the XRD patterns of BFY*x* samples. The diffraction profiles reveal that the BFY*x* oxides crystallize in a cubic perovskite structure with *Pm*-3*m* space group. The magnified XRD patterns between 29 and 33° are presented in Figure 1a. The diffraction peaks gradually shift to a lower angle direction with increasing the doping fraction, indicating the expansion of the lattice constants. To further obtain the lattice constants of the materials, Rietveld refined XRD data of BFY10 samples are given in Figure 1b. The refined lattice constants of BFY*x* samples are summarized in Table 1. The increase in cell volume from 67.220 $Å^3$ (x = 0.05) to 69.148 $Å^3$ (x = 0.15) is identified, which is attributed to the larger ionic radius of Y^{3+} (0.90 Å) relative to that of Fe^{3+} (0.55 Å). This phenomenon indicates that the Fe sites in $BaFeO_3$ are partially replaced by the Y ions. Furthermore, to examine the chemical compatibility between electrode and electrolyte, the mixtures of BFY*x* and CGO were co-fired at 1000 °C for 12 h. Figure 1c presents the XRD patterns of the calcined BFY*x*-CGO mixtures. No obvious impurities can be detected, revealing the favorable chemical compatibility of the BFY*x* cathodes with CGO electrolyte at 1000 °C.

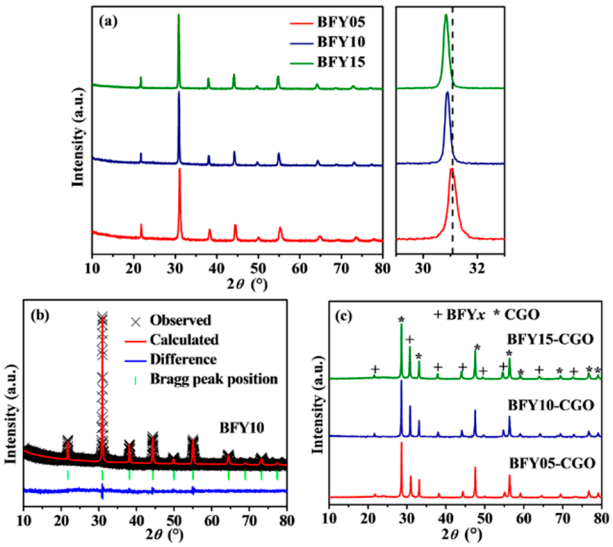

Figure 1. (**a**) Room temperature XRD patterns of BFY*x* samples and the magnified view of the XRD patterns, 2θ = 29 to 33°; (**b**) Rietveld refinement plot of BFY10 XRD data; (**c**) XRD patterns of BFY*x*-CGO composites fired at 1000 °C for 12 h.

Table 1. Lattice parameters of BFY*x* samples.

Space Group	x = 0.05	x = 0.1	x = 0.15
	Pm-3*m*	*Pm*-3*m*	*Pm*-3*m*
a (Å)	4.066	4.091	4.104
b (Å)	4.066	4.091	4.104
c (Å)	4.066	4.091	4.104
V ($Å^3$)	67.220	68.468	69.148
χ^2	2.171	1.906	4.190
R_{wp} (%)	7.762	7.664	9.811
R_P (%)	5.975	6.023	7.878

The oxygen mobility and reducibility of Fe ions for the BFY*x* samples were studied by O_2-TPD. Figure 2a presents the representative O_2-TPD profiles of the BFY*x* samples. The curves show two

desorption peaks at around 200 and 650 °C in all samples. The first broad peak located at ~200–300 °C is associated with the desorption process of the chemisorbed oxygen on the material surface. The second oxygen desorption peak may be ascribed to the reduction of Fe^{4+} to Fe^{3+} at 300–650 °C [23]. It is noteworthy that the BFY10 material shows the largest area of second desorption peak among the BFY*x* samples, indicating the highest oxygen vacancy concentration and favorable oxygen mobility of the BFY10. The oxygen non-stoichiometry (δ) of the BFY*x* samples at elevated temperatures was explored by TGA in air, as presented in Figure 2b. The δ values were determined by TGA results and the initial oxygen non-stoichiometry (δ_0) values at room temperature were obtained by the iodometric titration. The initial weight loss from room temperature to 300 °C is associated with the evaporation of adsorbed water. When the temperature is above 300 °C, the obvious weight loss is due to the reduction of Fe^{4+} to Fe^{3+}. It can be seen that the δ values of the samples decreases with the doping content from room temperature to 600 °C. However, when increasing the temperature to 600 °C, the BFY10 possesses the largest oxygen vacancy concentration, meaning its excellent oxygen ions mobility and promoted catalytic activity for ORR.

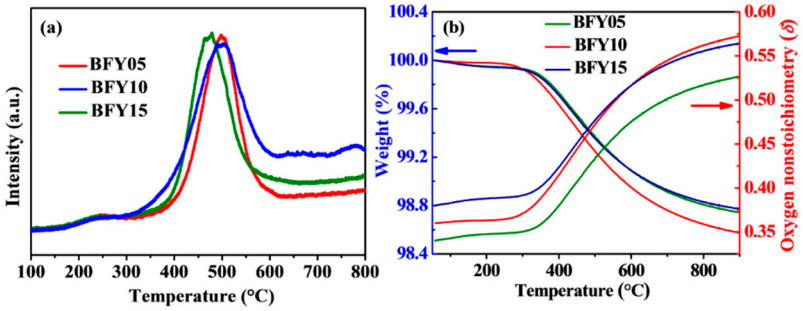

Figure 2. (**a**) TPD curves of BFY*x* samples measured from 100 to 800 °C; (**b**) TG curves and oxygen non-stoichiometry (δ) of BFY*x* between 50 and 900 °C.

The temperature dependence of electrical conductivity for the BFY*x* samples within the temperature range of 100–800 °C in air is presented in Figure 3a. The electrical conductivity of all samples shows a similar trend as a function of temperature. When increasing the temperature, the electrical conductivity of BFY*x* initially increases and reaches a maximum value at about 400 °C, and subsequently decreases between 400 and 800 °C. This indicates a transition from semi-conducting behavior to metal-like conduction. In addition, it is observed that the electrical conductivity gradually decreases with increasing Y-doping fraction. This phenomenon may be due to the higher Y content leads to the reduction of Fe^{4+} to Fe^{3+} or Fe^{2+} for the charge compensation, resulting in a decrease in the electrical conductivity. The maximum values of electrical conductivity are 9.81, 5.03, and 1.67 S cm^{-1} for BFY05, BFY10 and BFY15, respectively. These values are comparable to those of other reported $BaFeO_{3-\delta}$-based cathodes, such as $BaFe_{0.95}Nb_{0.05}O_{3-\delta}$ (9.5 S cm^{-1}) [16], $BaFe_{0.95}Zr_{0.05}O_{3-\delta}$ (7.5 S cm^{-1}) [14] and $BaFe_{0.8}In_{0.2}O_{3-\delta}$ (2.3 S cm^{-1}) [19]. Furthermore, the Arrhenius plots of electrical conductivity are presented in Figure 3b. The calculated activation energies (E_a) of BFY*x* are 0.29, 0.38, and 0.43 eV for BFY05, BFY10 and BFY15, respectively.

The EIS spectra were used to demonstrate electrocatalytic performance of the symmetric cells of BFY*x*|CGO|BFY*x*. Figure 4a displays the Nyquist plots of the BFY*x* cathodes at 700 °C in air. In general, the polarization resistance (R_p) value of the electrode is a crucial descriptor for the cathode performance, and the lower R_p value means a superior electrochemical activity for ORR. The R_p of BFY05, BFY10 and BFY15 cathodes are 0.136, 0.057, and 0.107 Ω cm^2 at 700 °C, respectively, suggesting highly electrocatalytic performance of the BFY*x* cathodes. The R_p value (700 °C) of BFY10 cathode is smaller than that of the Fe-based perovskite electrodes (Figure 4b) [24–27]. Furthermore, the Arrhenius plots of the polarization resistance are presented in Figure 4c. The calculated E_a values are 1.40, 1.33 and 1.45 eV for BFY05, BFY10, and BFY15, respectively. Moreover, the BFY10 cathode presents the lowest E_a value, implying the highest electrocatalytic performance.

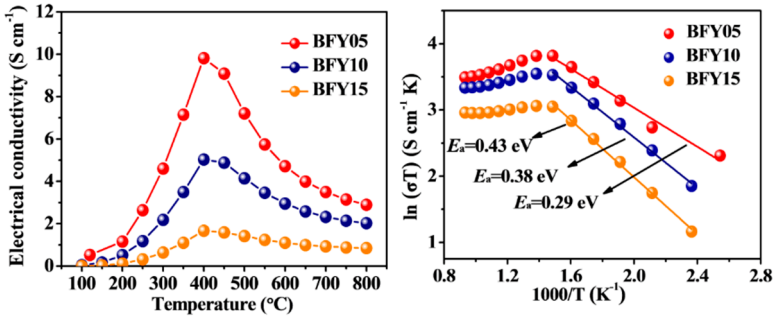

Figure 3. (**a**) The electrical conductivity of BFY*x* samples at 100–800 °C; (**b**) Arrhenius plots of BFY*x* with temperature.

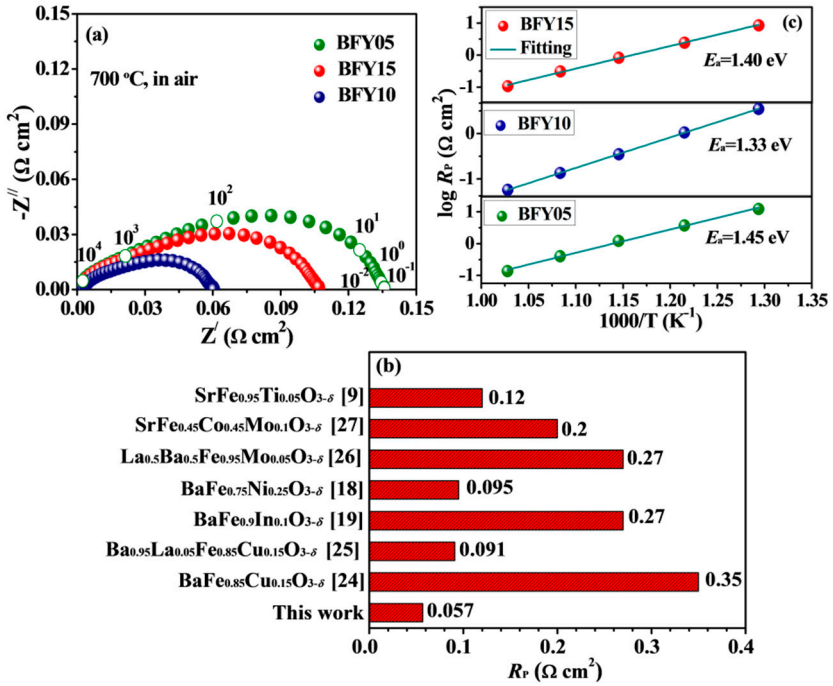

Figure 4. (**a**) Impedance spectra of BFY*x* measured at 700 °C; (**b**) Comparison of R_P for different Fe-based perovskite cathodes at 700 °C; (**c**) Arrhenius plots of R_p for BFY*x* cathodes.

To further clarify the electrochemical processes of the cathode, EIS spectra of the BFY10 electrode are systematically studied under varied Po_2 at 700 °C, as shown in Figure 5a. Clearly, the impedance spectra are consisted of three separable high-frequency, intermediate-frequency and low-frequency arcs, respectively, suggesting that the three different electrode processes occur on the cathode. The EIS data are further fitted with an equivalent circuit using the model of [R_{ohm}-(R_H-CPE$_H$)-(R_M-CPE$_M$)-(R_L-CPE$_L$)] (inset in Figure 5a) and analyzed by the distribution of relaxation time (DRT) method. Figure 5b displays the DRT results of BFY10 cathode under different Po_2 at 700 °C. It can be seen that the typical DRT plots presents three distinct peaks, the high-frequency peak P1 (HF), and intermediate-frequency peak P2 (MF) and low-frequency peak P3 (LF), corresponding to charge transport process, adsorption-dissociation process of oxygen molecule, and gaseous diffusion, respectively [28,29]. Additionally, the relationship between R_p and PO_2 can be expressed by the following formula: $R_p = k(PO_2)^{-m}$ (1) [30,31]. The dependence of the R_{HF}, R_{MF} and R_{LF} for the BFY10 cathode on the PO_2 at 700 °C is presented in Figure 5c. One should note that the m values are 0.26, 0.48, and 1.03 in high-frequency, intermediate-frequency and low-frequency region, respectively, which are ascribed to the charge transfer process ($O_{ads.} + 2e^{/} + V_{\ddot{O}} \Leftrightarrow O_O^x$, m = 1/4), the adsorption-dissociation of the oxygen molecule process ($O_{2,ads.} \Leftrightarrow 2O_{ads.}$, m = 1/2) and the adsorption and diffusion of gaseous oxygen on the electrode

surface ($O_2(g) \Leftrightarrow O_{2ads.}$, $m = 1$) [32]. Furthermore, it can be found that the R_{MF} is higher than R_{HF} and R_{LF}, implying that the rate-determining step for ORR is dominated by intermediate-frequency arc assigned to the oxygen adsorption-dissociation.

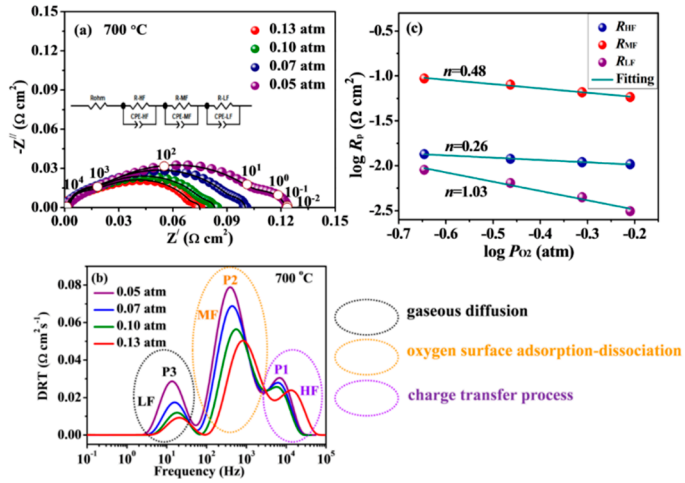

Figure 5. (**a**) Impedance spectra and (**b**) DRT results of BFY10 cathode under different oxygen partial pressure at 700 °C; (**c**) R_H, R_M, and R_L of BFY10 cathode as a function at 700 °C.

Some Ba-based cathodes for SOFCs show chemical instability under CO_2-containing atmospheres because of the formation of $BaCO_3$ on the cathode surface, diminishing oxygen reduction kinetics [33,34]. To evaluate the CO_2 tolerance of the electrode, EIS spectra of the BFY10 cathode were acquired in CO_2-containing air (3%, 5%, 10%) at 700 °C, as presented Figure 6a,b. It can be seen that the R_p value significantly increases with increasing the concentration of CO_2. However, the R_p recovers to the initial value after removing CO_2 atmosphere, which demonstrates the outstanding CO_2 tolerance of the BFY10 cathode. Generally, the average metal oxide binding energy (ABE) is normally used to assess the CO_2 durability of the cathode materials [35]. More negative ABE value indicates that oxide has excellent CO_2 tolerance. The ABE is calculated based on the following equation [36]:

$$\mathrm{ABE} = \mathrm{ABE(A\text{-}O)} + \mathrm{ABE(B\text{-}O)} \quad (2)$$

$$\mathrm{ABE(A-O)} = \frac{x_A}{12m}\left(\Delta_f H^o_{A_mO_n} - m\Delta H^o_A - \frac{n}{2}D_{O_2}\right) \quad (3)$$

$$\mathrm{ABE(B-O)} = \frac{x_B}{6m}\left(\Delta_f H^o_{B_mO_n} - m\Delta H^o_B - \frac{n}{2}D_{O_2}\right) \quad (4)$$

where x_A and x_B are the molar fraction of A and B metals; ΔH^o_A and ΔH^o_B are the sublimation heat of A and B metals; $\Delta_f H^o_{A_mO_n}$ and $\Delta_f H^o_{B_mO_n}$ are the formation heat of A_mO_n and B_mO_n oxides, and D_{O2} is the dissociation energy of O_2. The ABE values of BFYx oxides are −287.18 kJ mol^{-1}, −291.35 kJ mol^{-1}, and −295.51 kJ mol^{-1}, respectively, which are higher than cobalt-free perovskite cathodes, such as $Ba_{0.5}Sr_{0.5}Co_{0.8}Fe_{0.2}O_{3-\delta}$ (−274 kJ mol^{-1}) [37], $Bi_{0.5}Sr_{0.5}FeO_{3-\delta}$ (−276.67 kJ mol^{-1}) and $Bi_{0.5}Sr_{0.5}Fe_{0.9}Ta_{0.1}O_{3-\delta}$ (−296.97 kJ mol^{-1}) [26]. These results confirm that the BFYx cathodes have satisfactory CO_2 tolerance.

To further demonstrate the practical application of the BFYx cathodes, the single cells were fabricated and tested. Figure 7a–c displays the *I*–*V* and *I*–*P* curves of the single cells with the BFYx cathodes 600–700 °C using humidified hydrogen and air as the fuel and oxidant, respectively. At 700 °C, the peak powder densities of 0.73, 1.1, and 0.89 W cm^{-2} are achieved in the BFY05, BFY10 and BFY15 cathodes, respectively. It should be noted that the single cell with the BFY10 cathode shows the highest peak powder density among the BFYx electrodes, which is associated with superior electrochemical performance for ORR. In addition, the peak powder density of single cell with the BFY10 cathode is

higher than those of other cobalt-free perovskite cathodes [38–44]. Furthermore, Figure 7d displays the operating stability of the fuel cell with the BFY10 cathode during a period of 120 h. The single cell presents a stable current density and peak power density under an output voltage of 0.5 V without noticeable attenuation, suggesting that the BFY10 electrode has outstanding durability during the operating process. The remarkable electrocatalytic properties indicate that the BFY10 oxide is a highly attractive cathode candidate for SOFCs.

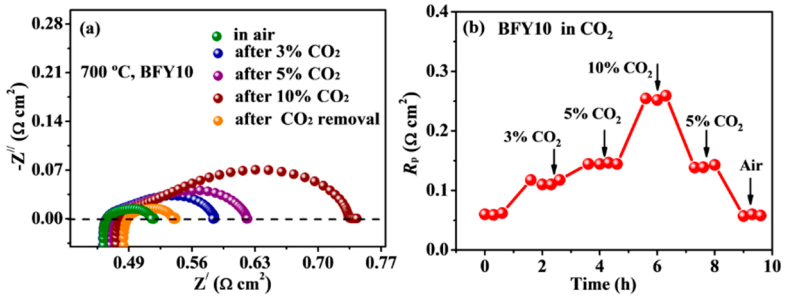

Figure 6. (**a**) Impedance spectra and (**b**) short-term stability of BFY10 cathode in various CO_2 concentrations at 700 °C.

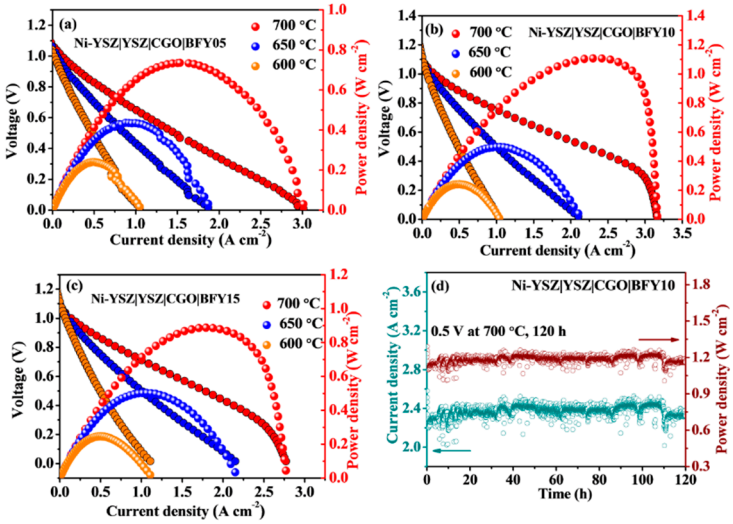

Figure 7. (**a**–**c**) *I*–*V* and *I*–*P* curves of the single cells with BFY*x* cathodes at 600–700 °C; (**d**) Stability test of the single cell with BFY10 cathode under an output voltage of 0.5 V.

4. Conclusions

In summary, Fe-based perovskite $BaFe_{1-x}Y_xO_{3-\delta}$ oxides with excellent ORR performance and CO_2 durability are evaluated as the cathode materials for SOFCs. Benefiting from cubic perovskite structure and large oxygen vacancy concentration, the BFY10 cathode presents outstanding electrochemical activity for ORR with a lower R_P value of 0.057 Ω cm^2 at 700 °C. In addition, the single fuel with the BFY10 cathode delivers a peak powder density of 1.1 W cm^{-2} at 700 °C, along with negligible attenuation over a period of 120 h. Furthermore, DRT study verifies that the adsorption-dissociation of the oxygen molecule process is the rate-limiting step on the cathode.

Author Contributions: D.M., Q.L., and H.Z. conceived and designed the experiments, and performed the experiments; J.G. and T.X. analyzed the data; L.S. and L.H. contributed reagents/materials/analysis tools; D.M. and Q.L. wrote the paper. All authors have read and agreed to the published version of the manuscript.

Funding: The project was supported by National Natural Science Foundation of China (51672072, 51972100) and Heilongjiang Provincial Fund for Distinguished Young Scholars (JC2018014).

Conflicts of Interest: The authors declare no conflict of interest.

References

1. Fan, L.; Zhu, B.; Su, P.-C.; He, C. Nanomaterials and technologies for low temperature solid oxide fuel cells: Recent advances, challenges and opportunities. *Nano Energy* **2018**, *45*, 148–176. [CrossRef]
2. Choudhury, A.; Chandra, H.; Arora, A. Application of solid oxide fuel cell technology for power generation—A review. *Renew. Sustain. Energy Rev.* **2013**, *20*, 430–442. [CrossRef]
3. Steele, B.C.H.; Heinzel, A. Materials for fuel-cell technologies. *Nat. Cell Biol.* **2001**, *414*, 345–352. [CrossRef]
4. Liu, P.; Luo, Z.F.; Kong, J.R.; Yang, X.F.; Liu, Q.C.; Xu, H. $Ba_{0.5}Sr_{0.5}Co_{0.8}Fe_{0.2}O_{3-\delta}$-based dual-gradient cathodes for solid oxide fuel cells. *Ceram. Int.* **2018**, *44*, 4516–4519. [CrossRef]
5. Ding, H.; Xue, X. $PrBa_{0.5}Sr_{0.5}Co_2O_{5+\delta}$ layered perovskite cathode for intermediate temperature solid oxide fuel cells. *Electrochim. Acta* **2010**, *55*, 3812–3816. [CrossRef]
6. Stambouli, A.; Traversa, E. Solid oxide fuel cells (SOFCs): A review of an environmentally clean and efficient source of energy. *Renew. Sustain. Energy Rev.* **2002**, *6*, 433–455. [CrossRef]
7. Chen, Y.; Wang, F.; Chen, D.; Dong, F.; Park, H.J.; Kwak, C.; Shao, Z. Role of silver current collector on the operational stability of selected cobalt-containing oxide electrodes for oxygen reduction reaction. *J. Power Sources* **2012**, *210*, 146–153. [CrossRef]
8. Zhou, W.; Shao, Z.; Ran, R.; Jin, W.; Xu, N. A novel efficient oxide electrode for electrocatalytic oxygen reduction at 400–600 °C. *Chem. Commun.* **2008**, *44*, 5791–5793. [CrossRef] [PubMed]
9. Yu, X.; Long, W.; Jin, F.; He, T. Cobalt-free perovskite cathode materials $SrFe_{1-x}Ti_xO_{3-\delta}$ and performance optimization for intermediate-temperature solid oxide fuel cells. *Electrochim. Acta* **2014**, *123*, 426–434. [CrossRef]
10. Rehman, A.U.; Li, M.; Knibbe, R.; Khan, M.S.; Peterson, V.K.; Brand, H.E.A.; Li, Z.; Zhou, W.; Zhu, Z. Enhancing Oxygen Reduction Reaction Activity and CO_2 Tolerance of Cathode for Low-Temperature Solid Oxide Fuel Cells by in Situ Formation of Carbonates. *ACS Appl. Mater. Interfaces* **2019**, *11*, 26909–26919. [CrossRef]
11. Liou, Y.C.; Chen, Y.R. Synthesis and microstructure of (LaSr)MnO_3 and (LaSr)FeO_3 ceramics by a reaction-sintering process. *Ceram. Int.* **2008**, *34*, 273–278.
12. Dong, F.; Chen, D.; Chen, Y.; Zhao, Q.; Shao, Z. La-doped $BaFeO_{3-\delta}$ perovskite as a cobalt-free oxygen reduction electrode for solid oxide fuel cells with oxygen-ion conducting electrolyte. *J. Mater. Chem.* **2012**, *22*, 15071–15079. [CrossRef]
13. Baiyee, Z.M.; Chen, C.; Ciucci, F. A DFT+U study of A-site and B-site substitution in $BaFeO_{3-\delta}$. *Phys. Chem. Chem. Phys.* **2015**, *17*, 23511–23520. [CrossRef]
14. Wang, J.; Saccoccio, M.; Chen, D.J.; Gao, Y.; Chen, C.; Ciucci, F. The effect of A-site and B-site substitution on $BaFeO_{3-\delta}$: An investigation as a cathode material for intermediate-temperature solid oxide fuel cells. *J. Power Sources* **2015**, *297*, 511–518. [CrossRef]
15. Dong, F.; Ni, M.; He, W.; Chen, Y.; Yang, G.; Chen, D.; Shao, Z. An efficient electrocatalyst as cathode material for solid oxide fuel cells: $BaFe_{0.95}Sn_{0.05}O_{3-\delta}$. *J. Power Sources* **2016**, *326*, 459–465. [CrossRef]
16. Dong, F.; Chen, Y.; Ran, R.; Chen, D.; Tadé, M.O.; Liu, S.; Shao, Z. $BaNb_{0.05}Fe_{0.95}O_{3-\delta}$ as a new oxygen reduction electrocatalyst for intermediate temperature solid oxide fuel cells. *J. Mater. Chem. A* **2013**, *1*, 9781–9791. [CrossRef]
17. Wang, J.; Lam, K.Y.; Saccoccio, M.; Gao, Y.; Chen, D.; Ciucci, F. Ca and in co-doped $BaFeO_{3-\delta}$ as a cobalt-free cathode material for intermediate-temperature solid oxide fuel cells. *J. Power Sources* **2016**, *324*, 224–232. [CrossRef]
18. Gao, L.; Zhu, M.Z.; Xia, T.; Li, Q.; Li, T.S.; Zhao, H. Ni-doped $BaFeO_{3-\delta}$ perovskite oxide as highly active cathode electrocatalyst for intermediate-temperature solid oxide fuel cells. *Electrochim. Acta* **2018**, *289*, 428–436.
19. Lu, Y.; Zhao, H.L.; Cheng, X.; Jia, Y.B.; Du, X.F.; Fang, M.Y.; Du, Z.H.; Zheng, K.; Świerczek, K. Investigation of In-doped $BaFeO_{3-\delta}$ perovskite-type oxygen permeable membranes. *J. Mater. Chem. A* **2015**, *3*, 6202–6214. [CrossRef]
20. Liu, X.T.; Zhao, H.L.; Yang, J.Y.; Li, Y.; Chen, T.; Lu, X.G. Lattice characteristics, structure stability and oxygen permeability of $BaFe_{1-x}Y_xO_{3-\delta}$ ceramic membranes. *J. Membr. Sci.* **2011**, *383*, 235–240.

21. Lu, Y.; Zhao, H.L.; Chang, X.W.; Du, X.F.; Li, K.; Ma, Y.H.; Yi, S.; Du, Z.H.; Zheng, K.; Świerczek, K. Novel cobalt-free $BaFe_{1-x}Gd_xO_{3-\delta}$ perovskite membranes for oxygen separation. *J. Mater. Chem. A* **2016**, *4*, 10454–10466.
22. Gao, L.; Li, Q.; Sun, L.P.; Zhang, X.F.; Huo, L.H.; Zhao, H.; Grenier, J. A novel family of Nb-doped $Bi_{0.5}Sr_{0.5}FeO_{3-\delta}$ perovskite as cathode material for intermediate-temperature solid oxide fuel cells. *J. Power Sources* **2017**, *371*, 86–95. [CrossRef]
23. Lu, F.; Xia, T.; Li, Q.; Wang, J.; Huo, L.; Zhao, H. Heterostructured simple perovskite nanorod-decorated double perovskite cathode for solid oxide fuel cells: Highly catalytic activity, stability and CO_2-durability for oxygen reduction reaction. *Appl. Catal. B Environ.* **2019**, *249*, 19–31. [CrossRef]
24. Zhu, M.; Cai, Z.; Xia, T.; Li, Q.; Huo, L.; Zhao, H. Cobalt-free perovskite $BaFe_{0.85}Cu_{0.15}O_{3-\delta}$ cathode material for intermediate-temperature solid oxide fuel cells. *Int. J. Hydrog. Energy* **2016**, *41*, 4784–4791. [CrossRef]
25. Xia, W.W.; Li, Q.; Sun, L.P.; Huo, L.H.; Zhao, H. Enhanced electrochemical performance and CO_2 tolerance of $Ba_{0.95}La_{0.05}Fe_{0.85}Cu_{0.15}O_{3-\delta}$ as Fe-based cathode electrocatalyst for solid oxide fuel cells. *J. Eur. Ceram. Soc.* **2020**, *40*, 1967–1974. [CrossRef]
26. Cai, H.D.; Xu, J.S.; Wu, M.; Long, W.; Zhang, L.; Song, Z.Y.; Zhang, L.L. A novel cobalt-free $La_{0.5}Ba_{0.5}Fe_{0.95}Mo_{0.05}O_{3-\delta}$ electrode for symmetric solid oxide fuel cell. *J. Eur. Ceram. Soc.* **2020**, *40*, 4361–4365. [CrossRef]
27. Zapata-Ramírez, V.; Mather, G.C.; Azcondo, M.T.; Amador, U.; Pérez-Coll, D. Electrical and electrochemical properties of the Sr(Fe,Co,Mo)$O_{3-\delta}$ system as air electrode for reversible solid oxide cells. *J. Power Sources* **2019**, *437*, 226895. [CrossRef]
28. Cai, W.; Guo, Y.; Zhang, T.; Guo, T.; Chen, H.; Lin, B.; Ou, X.; Liu, X. Characterization and polarization DRT analysis of a stable and highly active proton-conducting cathode. *Ceram. Int.* **2018**, *44*, 14297–14302. [CrossRef]
29. Xia, J.; Wang, C.; Wang, X.F.; Bi, L.; Zhang, Y.X. A perspective of DRT analysis for electrodes in solid oxide cells. *Electrochim. Acta* **2020**, *349*, 136328.
30. Li, S.L.; Zhang, L.K.; Xia, T.; Li, Q.; Sun, L.P.; Huo, L.H.; Zhao, H. Synergistic effect study of $EuBa_{0.98}Co_2O_{5+\delta}$-$Ce_{0.8}Sm_{0.2}O_{1.9}$ composite cathodes for intermediate-temperature solid oxide fuel cells. *J. Alloy. Comp.* **2019**, *771*, 513–521. [CrossRef]
31. Escudero, M.; Aguadero, A.; Alonso, J.; Daza, L. A kinetic study of oxygen reduction reaction on La_2NiO_4 cathodes by means of impedance spectroscopy. *J. Electroanal. Chem.* **2007**, *611*, 107–116. [CrossRef]
32. Takeda, Y.; Kanno, R.; Noda, M.; Tomida, Y.; Yamamoto, O. Cathodic Polarization Phenomena of Perovskite Oxide Electrodes with Stabilized Zirconia. *J. Electrochem. Soc.* **1987**, *134*, 2656–2661. [CrossRef]
33. Li, J.; Huo, J.; Lu, Y.; Wang, Q.; Xi, X.; Fan, Y.; Fu, X.Z.; Luo, J.L. Ca-containing $Ba_{0.95}Ca_{0.05}Co_{0.4}Fe_{0.4}Zr_{0.1}Y_{0.1}O_{3-\delta}$ cathode with high CO_2-poisoning tolerance for proton-conducting solid oxide fuel cells. *J. Power Sources* **2020**, *453*, 227909. [CrossRef]
34. Bucher, E.; Egger, A.; Caraman, G.B.; Sitte, W. Stability of the SOFC cathode materials (Ba,Sr)(Co,Fe)$O_{3-\delta}$ in CO_2-containing atmospheres. *J. Electrochem. Soc.* **2008**, *155*, B1218–B1224. [CrossRef]
35. Gu, H.; Sunarso, J.; Yang, G.; Zhou, C.; Song, Y.; Zhang, Y.; Wang, W.; Ran, R.; Zhou, W.; Shao, Z. Turning Detrimental Effect into Benefits: Enhanced Oxygen Reduction Reaction Activity of Cobalt-Free Perovskites at Intermediate Temperature via CO_2-Induced Surface Activation. *ACS Appl. Mater. Interfaces* **2020**, *12*, 16417–16425. [CrossRef]
36. Zhang, Y.; Yang, G.; Chen, G.; Ran, R.; Zhou, W.; Shao, Z. Evaluation of the CO_2 Poisoning Effect on a Highly Active Cathode $SrSc_{0.175}Nb_{0.025}Co_{0.8}O_{3-\delta}$ in the Oxygen Reduction Reaction. *ACS Appl. Mater. Interfaces* **2016**, *8*, 3003–3011. [CrossRef]
37. Zhu, Y.; Zhou, W.; Chen, Y.; Shao, Z. An Aurivillius Oxide Based Cathode with Excellent CO_2 Tolerance for Intermediate-Temperature Solid Oxide Fuel Cells. *Angew. Chem.* **2016**, *128*, 9134–9139. [CrossRef]
38. Wang, S.F.; Yeh, C.T.; Wang, Y.R.; Hsu, Y.F. Effect of (LaSr)(CoFeCu)$O_{3-\delta}$ cathodes on the characteristics of intermediate temperature solid oxide fuel cells. *J. Power Sources* **2012**, *201*, 18–25. [CrossRef]
39. Shi, H.; Ding, Z.; Ma, G. Electrochemical Performance of Cobalt-free $Nd_{0.5}Ba_{0.5}Fe_{1-x}Ni_xO_{3-\delta}$ Cathode Materials for Intermediate Temperature Solid Oxide Fuel Cells. *Fuel Cells* **2016**, *16*, 258–262. [CrossRef]
40. Zhu, Z.; Wei, Z.; Zhao, Y.; Chen, M.; Wang, S. Properties characterization of tungsten doped strontium ferrites as cathode materials for intermediate temperature solid oxide fuel cells. *Electrochim. Acta* **2017**, *250*, 203–211. [CrossRef]

41. Song, X.Q.; Le, S.R.; Zhu, X.D.; Qin, L.; Luo, Y.; Li, Y.W.; Sun, K.N.; Chen, Y. High performance $BaFe_{1-x}Bi_xO_{3-\delta}$ as cobalt-free cathodes for intermediate temperature solid oxide fuel cell. *Int. J. Hydrog. Energy* **2017**, *42*, 15808–15817. [CrossRef]
42. Ren, R.; Wang, Z.; Meng, X.; Xu, C.; Qiao, J.; Sun, W.; Sun, K. Boosting the Electrochemical Performance of Fe-Based Layered Double Perovskite Cathodes by Zn^{2+} Doping for Solid Oxide Fuel Cells. *ACS Appl. Mater. Interfaces* **2020**, *12*, 23959–23967. [CrossRef] [PubMed]
43. Xie, D.; Guo, W.; Guo, R.; Liu, Z.; Sun, D.; Meng, L.; Zheng, M.; Wang, B. Synthesis and electrochemical properties of $BaFe_{1-x}Cu_xO_{3-\delta}$ perovskite oxide for IT-SOFC cathode. *Fuel Cells* **2016**, *16*, 829–838. [CrossRef]
44. Ni, W.; Zhu, T.; Chen, X.; Zhong, Q.; Ma, W. Stable, efficient and cost-competitive Ni-substituted Sr $(Ti,Fe)O_3$ cathode for solid oxide fuel cell: Effect of A-site deficiency. *J. Power Sources* **2020**, *451*, 227762. [CrossRef]